The autophagy protein, ATG14 safeguards against unscheduled pyroptosis activation to enable embryo transport during early pregnancy

Pooja Popli[1], Arin K. Oestreich[2,3], Vineet K. Maurya[4], Marina N. Rowen[2,3], Yong Zhang[5], Michael J. Holtzman[5], Ramya Masand[1], John Lydon[4], Shizuo Akira[6,7], Kelle H. Moley[2,3], and Ramakrishna Kommagani[1,8*]

[1]Department of Pathology and Immunology, Baylor College of Medicine, One Baylor Plaza, Houston, TX 77030, USA

[2]Department Obstetrics and Gynecology,
[3]Center for Reproductive Health Sciences, Washington University School of Medicine, St. Louis, MO, 63110, USA

[4]Department of Molecular and Cellular Biology, Baylor College of Medicine, One Baylor Plaza, Houston, TX 77030, USA

[5]Department of Medicine and Department of Cell Biology, Washington University School of Medicine, St. Louis, MO, 63110, USA

[6]Department of Host Defense, Research Institute for Microbial Diseases (RIMD),
[7]Laboratory of Host Defense, World Premier Institute Immunology Frontier Research Center (WPI-IFReC), Osaka University, Osaka 565-0871, Japan

[8]Department of Molecular Virology and Microbiology, Baylor College of Medicine, One Baylor Plaza, Houston, TX 77030, USA.

***Correspondence to:**

Ramakrishna Kommagani
Associate Professor
Department of Pathology and Immunology
Department of Molecular Virology and Microbiology
Alkek Center for Metagenomics and Microbiome Research
T228A, One Baylor Plaza
Baylor College of Medicine
Houston, TX, 77030
Email: Rama.Kommagani@bcm.edu
Phone: (713)-798-5085
Fax: 713-798-5838

Short title: Cellular self-digestion for female reproductive tract functions

The authors have declared that no conflict of interest exists.

35 **Non-standard Abbreviations**

36 WT: Wild Type

37 HESCs: Human Endometrial stromal cells

38 dpc: Days post coitum

39 E2: Estrogen

40 P4: Progesterone

41 VPS 15: Vacuolar sorting protein 15

42 cKO: Conditional knockout

43 FRT: Female reproductive tract

44 GSDMD: Gasdermin D

45 **Keywords:** fallopian tube, oviduct, embryo transport, uterus, pregnancy failure, infertility

Abstract

Recurrent pregnancy loss (RPL), characterized by two or more failed clinical pregnancies, poses a significant challenge to reproductive health. In addition to embryo quality and endometrial function, proper oviduct function is also essential for successful pregnancy establishment. Therefore, structural abnormalities or inflammation resulting from infection in the oviduct may impede the transport of embryos to the endometrium, thereby increasing the risk of miscarriage. However, our understanding of the biological processes that preserve the oviductal cellular structure and functional integrity is limited. Here, we report that Atg14-dependent autophagy plays a crucial role in maintaining the cellular integrity of the oviduct by controlling inflammatory responses, thereby supporting efficient embryo transport. Specifically, the conditional depletion of the autophagy-related gene, *Atg14* in the oviduct causes severe structural abnormalities compromising its cellular integrity leading to the abnormal retention of embryos. Interestingly, the selective loss of *Atg14* in oviduct ciliary epithelial cells did not impact female fertility, highlighting the specificity of ATG14 function in distinct cell types within the oviduct. Mechanistically, loss of *Atg14* triggered unscheduled pyroptosis via altering the mitochondrial integrity leading to inappropriate embryo retention and impeded embryo transport in the oviduct. Finally, pharmacological activation of pyroptosis in pregnant mice phenocopied the genetically induced defect and caused impairment in embryo transport. Together, we found that ATG14 safeguards against unscheduled pyroptosis activation to enable embryo transport from the oviduct to uterus for the successful implantation. Of clinical significance, these findings provide possible insights into the underlying mechanism(s) of early pregnancy loss and might aid in developing novel prevention strategies using autophagy modulators.

Introduction

A successful pregnancy is orchestrated by the sequential and coordinated events happening in the FRT [1]. Each of these events is crucial to advance to the next step in pregnancy. For example, as a first step, the ovary undergoes ovulation to release a mature ovum which is collected by oviduct fimbriae and funnelled through the infundibulum into the ampulla where they get fertilized by sperm. The embryos then pass through the ampulla-isthmus junction (AIJ) to enter the isthmus of the oviduct before exiting via the distal utero-tubal junction (UTJ) to implant on the wall of the uterus. Recently, the intricate structural and cellular diversity of the oviduct has drawn significant attention, emphasizing its vital role in facilitating embryo development and transport [2-4]. Morphologically, the oviduct is divided into four evolutionarily conserved regions: the infundibulum (nearest the ovary), ampulla (the site of fertilization), isthmus (serving as a sperm reservoir and site for early embryonic development), and utero-tubal junction (connected to the uterus). Each of these segments comprises epithelial, stromal, and smooth muscle cells with lumen lined up with an epithelium containing secretory ($PAX8^+$) and multi-ciliated ($FOXJ1^+$) cells. While the infundibulum and ampulla are composed of more ciliated than secretory cells, the isthmus has more secretory than ciliated cells [5, 6]. Successful pregnancy requires that the embryo transit the entire oviduct orchestrated by the following: (1) secretory cells producing oviduct fluid, (2) beating cilia to ensure unidirectional flow of the fluid, and (3) periodic contractions of surrounding muscle to propel fluid flow. Therefore, a combination of ciliary and muscular activity contributes to the overall success of oviduct embryo transport. This combination of ciliary and muscular activity plays a crucial role in the effective transport of the embryo through the oviduct. Any perturbations in these early pregnancy events can lead to adverse ripple effects that can compromise pregnancy outcomes. Previous studies have reported that impaired oviductal transport of embryos can lead to pregnancy failure and cause infertility in mice [7-10]. However, the underlying mechanism is not yet completely understood.

96 Autophagy is a cellular process, evolutionarily conserved from yeast to mammals, that
97 recycles long-lived proteins and organelles to maintain cell energy homeostasis. Autophagy
98 is classically activated through the nutrient sensor or mammalian target of the rapamycin
99 complex. Genetic screens for autophagy-defective mutants in yeast and other fungi have
100 currently identified 41 autophagy-related (ATG) genes that play a primary role in autophagy
101 [11, 12]. Approximately half of these genes have homologs in higher organisms, and *Atg14*
102 (also known as Barkor for Beclin 1 (*Becn1*)-associated autophagy-related key regulator) is
103 one of them [13, 14]. ATG14 is part of a protein complex that is composed of Beclin 1, vacuolar
104 sorting protein 15 (VPS15), and VPS34 (also named as Pik3c3, the catalytic subunit of the
105 class III phosphatidylinositol 3-kinase), and this ATG14-containing complex plays an important
106 role in the initiation process of autophagy.

107 Pyroptosis is a type of inflammatory cell death mediated by gasdermin (GSDM) and is
108 a product of continuous cell expansion until the cytomembrane ruptures, resulting in the
109 release of cellular contents that can activate strong inflammatory and immune responses.
110 Gasdermin family proteins are the primary executioners of pyroptosis. Cytotoxic N-terminal of
111 gasdermins generated from caspases mediated cleavage of gasdermin proteins oligomerizes
112 and forms pores across the cell membrane, leading to the release of proinflammatory
113 cytokines such as interleukin-1β (IL-1β) and interleukin-18 (IL-18). Aberrant activation of
114 pyroptosis has been implicated in the progression of many diseases including cancer and
115 autoimmune, cardiovascular, and infectious diseases [15-17]. Recent studies have shown that
116 the interactions between pyroptosis and autophagy play an important role in various
117 physiological and pathological processes [15-20]. For example, autophagy inhibition
118 upregulates galangin-induced pyroptosis in human glioblastoma multiforme cells and
119 promotes pneumococcus-induced pyroptosis [21, 22]. However, the studies defining the
120 molecular interactions between the pyroptosis, and autophagy pathways are very limited.

121 With a better understanding of the fundamental process of autophagy, its
122 pathophysiological functions have begun to be appreciated in the female reproductive tract.

123 For example, mice deficient in key autophagy genes such as genetic knockout of *Atg7* or
124 *Becn1* result in primary ovarian insufficiency and reduced progesterone production [23, 24].
125 Similarly, recent studies from our group established the roles of three different autophagy-
126 specific genes: ATG16L, FIP200/RB1CC1, or BECN1 in endometrial physiological processes,
127 including receptivity and decidualization [25-27]. However, none of these proteins exhibited
128 any discernible impact on oviduct function. Surprisingly, in this study, we revealed a critical
129 role for Atg14 in maintaining proper oviduct function, specifically enabling the transport of
130 embryos to the uterus- a function distinct from that of other autophagy-related proteins. Loss
131 of ATG14 in the oviduct resulted in severe structural abnormalities, compromising its cellular
132 integrity, ultimately leading to embryo retention and infertility.

133 **Materials and Methods**

134 **Animal care and use:**

135 All animal studies were approved by the Institutional Animal Care and Use Committee of
136 Washington University School of Medicine, Saint Louis, MO, USA and Use Committee of
137 Baylor College of Medicine, Houston, TX, USA. *Atg14* f/f mice were provided by gift from Dr.
138 Shizuo Akira at the Department of Host Defense, Research Institute for Microbial Diseases
139 (RIMD), Osaka University, and previously described [28]. Wild type Pr-cre mice were provided
140 by Dr. John Lydon at Baylor College of Medicine, Houston and previously described [29].
141 $Atg14^{flox/flox}$ mice, in which exon 4 was flanked by loxp sites, were bred to progesterone
142 receptor cre ($PR^{cre/+}$) mice to generate ($Atg14^{flox/flox}$; $PR^{cre/+}$ mice), hereafter referred to as *Atg14*
143 cKO mice. Both control and conditional knockout females were generated by crossing females
144 carrying homozygous $Atg14^{flox/flox}$ alleles with *Atg14* cKO males. *Foxj1-cre* mice were a
145 generous gift from Dr. Michael J. Holtzman at Washington University St. Louis and previously
146 described [30]. *Foxj1*/*Atg14* cKO mice were generated by crossing females carrying
147 homozygous $Atg14^{f/f}$/$Foxj1^{f/f}$ females with $Atg14^{f/f}$/*Foxj1-cre* males. All mice were age-
148 matched and on a C57BL/6 genetic background (The Jackson Laboratory, Bar Harbor, ME).
149 Mice were genotyped by PCR analysis of genomic DNA isolated from tail clippings using the
150 gene-specific primers listed in **Supplementary Table 1.**

151 **Fertility analysis and timed mating**

152 Female fertility was determined by mating cohorts of *Atg14* cKO experimental (n=6) and
153 control *Atg14* f/f (n=4) females individually starting at 8 weeks of age with sexually mature
154 males of proven fertility. Similarly, breeding trials were set up for *Foxj1/Atg14*-cre females
155 (n=6) and *Foxj1*/*Atg14* control 8-week-old f/f females (n=6). The numbers of litters and pups
156 were tracked over 6 months for each female. Pups per litter for each genotype are reported
157 as mean ± SEM. For timed mating, the morning on which the copulatory plug was first
158 observed was considered 1 dpc. To visualize implantation sites, mice received a tail vein

159 injection of 50 μL of 1% Chicago Sky Blue dye (Sigma-Aldrich, St. Louis, MO, USA) at 5 dpc
160 just before sacrifice.

161 **Steroid hormone treatments**

162 The hormonal profile of pregnancy at the time of implantation was done using a previously
163 described experimental scheme [26]. Briefly, *Atg14* cKO and control females (8 weeks old)
164 were bilaterally ovariectomized under ketamine anesthesia with buprenorphine-SR as an
165 analgesic. Mice were allowed to rest for two weeks to dissipate all endogenous ovarian
166 hormones. After the resting period, mice were injected with 100 ng of estrogen (E2; Sigma-
167 Aldrich) dissolved in 100 μL of sesame oil on two consecutive days and then allowed to rest
168 for two days. At this point, mice were randomly divided into three groups of five: Vehicle-
169 treated (E2 priming) mice received four consecutive days of sesame oil injections; E2 group
170 mice received three days of sesame oil injections followed by a single injection of 50 ng of E2
171 on the fourth day; The E2/P4 mice received 1 mg of progesterone (P4; Sigma-Aldrich) for
172 three consecutive days followed by a single injection of 1 mg P4 plus 50 ng E2 on the fourth
173 day. All hormones were delivered by subcutaneous injection in a 90:10 ratio of sesame oil:
174 ethanol. Mice were euthanized 16 hours after the final hormone injection to collect the uteri. A
175 small piece of tissue from one uterine horn was processed in 4% neutral buffered
176 paraformaldehyde for histology, and the remaining tissue was snap-frozen and stored at -80
177 °C.

178 **Hormone Analysis**

179 For serum hormone levels measurement, blood was collected from D4 pregnant mice before
180 mice were sacrificed. Serum was separated from the blood by centrifugation and stored at -
181 80°C before hormone analysis. Serum P4 and E2 levels were measured by using ELISA kits
182 (Enzo life Sciences) according to the manufacturer's instructions.

183 **Hematoxylin and eosin staining**

184 Tissues were fixed in 4% paraformaldehyde, embedded in paraffin, and then sectioned (5 μm)
185 with a microtome (Leica Biosystem, Wetzlar, Germany). Tissue sections were deparaffinized,
186 rehydrated, and stained with Hematoxylin and Eosin (H&E) as described previously [31]. All
187 the histology was performed on three sections from each tissue of individual mice, and one
188 representative section image is shown in the respective figures.

189 **Histological analysis**

190 For histological analysis, the collected tissues (oviduct or uteri) were fixed in 4%
191 paraformaldehyde, embedded in paraffin, and sectioned. Sections (5 μm) were
192 immunostained (n=5 per group) as described previously [31]. Briefly, after deparaffinization,
193 sections were rehydrated in an ethanol gradient and then boiled for 20 min. in citrate buffer
194 (Vector Laboratories Inc., Newark, CA, USA) for antigen retrieval. Endogenous peroxidase
195 activity was quenched with Bloxall (Vector Laboratories Inc.), and tissues were blocked with
196 2.5% goat serum in PBS for 1 hr (Vector Laboratories Inc.). After washing in PBS three times,
197 tissue sections were incubated overnight at 4 °C in 2.5% goat serum containing the primary
198 antibodies listed in **Supplementary Table 2.** Sections were incubated for 1 hr with biotinylated
199 secondary antibody, washed, and incubated for 45 min with ABC reagent (Vector Laboratories
200 Inc.). Color was developed with 3, 3'-diaminobenzidine (DAB) peroxidase substrate (Vector
201 Laboratories Inc.), and sections were counter-stained with hematoxylin. Finally, sections were
202 dehydrated and mounted in Permount histological mounting medium (Thermo Fisher
203 Scientific, Waltham, MA, USA).

204 **Transmission electron microscopy (TEM)**

205 For ultrastructural analysis, oviducts were fixed in 2% paraformaldehyde/2.5% glutaraldehyde
206 (Ted Pella Inc., Redding, CA) in 100 mM cacodylate buffer, pH 7.2 for 1 hr at room temperature
207 and then overnight at 4°C. Samples were washed in cacodylate buffer and postfixed in 1%
208 osmium tetroxide (Ted Pella Inc.) for 1 hr. Samples were then rinsed extensively in dH20 prior
209 to en bloc staining with 1% aqueous uranyl acetate (Ted Pella Inc.) for 1 hr. Following several
210 rinses in dH20, samples were dehydrated in a graded series of ethanol and embedded in

211 Eponate 12 resin (Ted Pella Inc.). For initial evaluation semithin sections (0.5 μm) were cut
212 with a Leica Ultracut UCT7 ultramicrotome (Leica Microsystems Inc., Bannockburn, IL) and
213 stained with toluidine blue. Sections of 95 nm were then cut and stained with uranyl acetate
214 and lead citrate and viewed on a JEOL 1200 EX II transmission electron microscope (JEOL
215 USA Inc., Peabody, MA). Images at magnifications of 3,000X to 30,000X were taken with an
216 AMT 8-megapixel digital camera (Advanced Microscopy Techniques, Woburn, MA).

217 **Immunofluorescence analysis**

218 Formalin-fixed and paraffin-embedded sections were deparaffinized in xylene, rehydrated in
219 an ethanol gradient, and boiled in a citrate buffer (Vector Laboratories Inc.) for antigen
220 retrieval. After blocking with 2.5% goat serum in PBS (Vector laboratories) for 1 hr at room
221 temperature, sections were incubated overnight at 4°C with primary antibodies
222 (**Supplementary Table 2**) diluted in 2.5% normal goat serum. After washing with PBS,
223 sections were incubated with Alexa Fluor 488-conjugated secondary antibodies (Life
224 Technologies, Carlsbad, CA, USA) for 1 hr at room temperature, washed, and mounted with
225 ProLong Gold Antifade Mountant with DAPI (Thermo Fisher Scientific). All
226 Immunofluorescence images were obtained using a Zeiss LSM 880 confocal microscope (10x
227 and 40x objective lens).

228 Fresh oviduct tissues from 8-week-old mice from control (n=3) and cKO (n=3) were
229 collected and fixed in 4 % PFA at 4ºC overnight. After that, oviducts were washed with PBS
230 and cryoprotected using gradually increased sucrose concentrations in a row (15 and 30%
231 w/v). 24 h later, oviducts were embedded in an OCT medium, frozen (−80 °C), and cryo-
232 sectioned in the CM3050S Cryostat (Leica Biosystems, Germany). The cryosections were
233 mounted on Superfrost plus glass slides (Fisher Scientific, Pittsburgh, PA) and stored at −80°C
234 until used.

235 Cryo-sections were processed for immunofluorescence staining as described before
236 [32]. Briefly, cryosections were blocked in 2.5% normal goat serum. After washing with PBS,

237 sections were blocked with Mouse on Mouse (M.O.M.) IgG blocking reagent (M.O.M.
238 Fluorescein Kit, Vector Laboratories, #FMK-2201) diluted in 1% BSA per the manufacturer's
239 instructions. After blocking, sections were incubated overnight at 4°C with primary antibodies
240 (**Supplementary Table 2**) diluted in 2.5% normal goat serum. Next day, following washing
241 with PBS, sections were incubated with Alexa Fluor 488-conjugated secondary antibodies
242 (Life Technologies, Carlsbad, CA, USA) for 1 hr at room temperature, washed, and mounted
243 with ProLong Gold Antifade Mountant with DAPI (Thermo Fisher Scientific). All
244 Immunofluorescence images were imaged using a Nikon Fluorescent microscope.

245 **Western blotting**

246 Protein lysates (40 µg per lane) from uteri or oviducts were loaded on a 4-15% SDS-PAGE
247 gel (Bio-Rad, Hercules, CA, USA), separated in 1X Tris-Glycine Buffer (Bio-Rad), and
248 transferred to PVDF membranes via a wet electro-blotting system (Bio-Rad), all according to
249 the manufacturer's directions [33]. PVDF membranes were blocked for 1 hour in 5% non-fat
250 milk in Tris-buffered saline containing 0.1% Tween-20 (TBS-T, Bio-Rad), then incubated
251 overnight at 4 °C with antibodies listed in **Supplementary Table 2** in 5% BSA in TBS-T. Blots
252 were then probed with anti-Rabbit IgG conjugated with horseradish peroxidase (1:5000, Cell
253 Signaling Technology, Danvers, MA, USA) in 5% BSA in TBS-T for 1 hr at room temperature.
254 Signal was detected with the Pierce™ ECL Western Blotting Substrate (Millipore, Billerica,
255 MA, USA), and blot images were collected with a Bio-Rad ChemiDoc imaging system.

256 **RNA Isolation and Quantitative Real-Time RT-PCR Analysis**

257 Tissues/cells were lysed in RNA lysis buffer, and total RNA was extracted with the Purelink
258 RNA mini kit (Invitrogen, Carlsbad, CA, USA) according to the manufacturer's instructions.
259 RNA was quantified with a Nano-Drop 2000 (Thermo Fisher Scientific). Then, 1 µg of RNA
260 was reverse transcribed with the High-Capacity cDNA Reverse Transcription Kit (Thermo
261 Fisher Scientific). The amplified cDNA was diluted to 10 ng/µL, and qRT-PCR was performed
262 with primers listed in the **Supplementary Table 1** and TaqMan 2X master mix (Applied
263 Biosystems/Life Technologies, Grand Island, NY, USA) on a 7500 Fast Real-time PCR system

264 (Applied Biosystems/Life Technologies). The delta-delta cycle threshold method was used to
265 normalize expression to the reference gene 18S.

266 **Treatment of mice with Polyphyllin VI**

267 Polyphyllin VI (Selleck chemicals, Houston, TX, USA), a pharmacological agent that induces
268 caspase-1-mediated pyroptosis, was used to study its effects on embryo transport in the
269 oviduct [34]. Eight-week-old C57BL/6 mice were injected for three consecutive days starting
270 from 1 dpc with Polyphyllin VI activator dissolved in 40% PEG-300 (15mg/kg body weight).
271 Dimethyl sulfoxide with 40% PEG-300 was administered as a vehicle.

272 **Statistics**

273 A two-tailed paired student t-test was used to analyze data from experiments with two
274 experimental groups and one-way ANOVA followed by Tukey's post hoc multiple range test
275 was used for multiple comparisons. All data are presented as mean ±SEM. GraphPad Prism
276 9 software was used for all statistical analyses. Statistical tests, including p values, are
277 reported in the corresponding figure legends or, when possible, directly on the data image. To
278 ensure the reproducibility of our findings, experiments were replicated in a minimum of three
279 independent samples, to demonstrate biological significance, and at least three independent
280 times to ensure technical and experimental rigor and reproducibility.
281

282 **Results**

283 **Conditional deletion of *Atg14* in the FRT results in infertility despite the normal ovarian**
284 **function**

285 To explore the role of *Atg14* in uterine function, we first determined its expression
286 levels in uterus during early pregnancy (Day 1-7) in mice. We found distinct expression of
287 ATG14 in all the uterine compartments (luminal epithelium, glands, and stroma) by day 1 of
288 pregnancy, which disappeared by day 2 of pregnancy (**Fig. 1A**). However, the ATG14
289 expression in uterus reappeared by day 3 and persisted through the day 7 of pregnancy. The
290 period from day 3 to day 7 is critical, as it is during this time when uterus begins to prepare for
291 embryo implantation and undergoes decidualization process. Consistent with protein
292 expression, similar *Atg14* expression at mRNA levels was noted in uteri from early pregnant
293 mice (**Fig. 1B**). This analysis suggests a potential role for ATG14 protein in the uterine
294 physiologic adaptations during early pregnancy. Thus, to study the role of ATG14 in uterine
295 function, we generated a conditional knockout ($PR^{cre/+}$ /$Atg14^{flox/flox}$) mouse model by crossing
296 *Atg14* flox/flox mice with mice expressing Cre recombinase under the control of progesterone
297 receptor promoter ($PR^{cre/+}$). Histological examination of the uterus from adult females showed
298 no gross morphological differences between *Atg14* cKO and control mice (**Fig. S1A**). Further,
299 we did not find any overt defects in ovary as cKO mice had normal follicles and corpus luteum
300 as like their corresponding controls (**Fig. S1B**). Analysis of transcript levels from the uterus,
301 ovary, and liver showed that while *Atg14* levels were efficiently depleted in uteri from cKO
302 mice the levels were unaltered in the ovary and liver samples in control and cKO mice (**Fig.**
303 **1C**). Immunofluorescence analysis further confirmed the efficient deletion of ATG14 in all
304 uterine compartments (epithelium and stroma) of cKO mice uteri compared to corresponding
305 control groups (**Fig. 1D**).

306 Considering the effective ablation, a 6-month breeding study was performed mating
307 virile wild-type male mice with adult *Atg14* cKO and control female mice. We found that *Atg14*
308 cKO females did not deliver any litter during the 6-months trial period. However, the control
309 female (*Atg14* flox/flox) mice delivered an average of ~7-8 pups per litter every month (**Table**

310 **1**) (**Fig. 1E).** These findings suggest an indispensable role of *Atg14* in female fertility with intact
311 ovarian function.

312 **Loss of *Atg14* results in impaired embryo implantation and uterine receptivity in mice**

313 Based on the normal ovarian morphology, we posited that the infertility observed in
314 females with *Atg14* cKO status could be attributed to compromised uterine functioning.
315 Analysis of the implanting embryos at Day 5 of pregnancy showed no implantation sites in the
316 uteri of *Atg14* cKO females, whereas ~8 to 9 implantation sites were seen in the uteri of control
317 mice at 5 dpc (**Fig. 2A, left panel**). Whilst there was no embryo present in the uterine lumen
318 of *Atg14* cKO mice, a fully attached embryo encapsulated by the luminal uterine epithelium,
319 was seen in control mice uteri (**Fig. 2A, middle panel**). Additionally, MUC1, a receptive
320 marker expression persisted in the luminal epithelium of cKO mice uteri at 5 dpc as well as 4
321 dpc (**Fig. 2A, right panel, Fig. 2C**). The process of successful embryo attachment and
322 implantation within the uterus necessitates a transition from a non-receptive to a receptive
323 state, a transformation orchestrated under the regulated influence of steroid hormones. Thus,
324 the effects of *Atg14* loss on uterine responsiveness to steroid hormones E2 and P4 were
325 characterized. We performed an established hormone-induced uterine receptivity experiment,
326 which involved ordered and co-stimulatory actions of E2 and P4 leading to the initiation of a
327 receptive phase [35]. In response to E2 treatment, uteri from both *Atg14* control and cKO mice
328 showed similar proliferation as evidenced by Ki-67 staining (**Fig. 2B, middle panel**). Following
329 the co-stimulation with E2+P4 treatment, epithelial proliferation was inhibited with concomitant
330 induction of stromal cell proliferation in control mice uteri indicating fully receptive uteri (**Fig.
331 2B**). Interestingly, cKO mice uteri failed to elicit sub-epithelial stromal cell proliferation and
332 showed intact P4-driven inhibition of epithelial proliferation. Consistently, uteri from *Atg14* cKO
333 mice at 4 dpc showed a reduced number of proliferating stromal cells (**Fig. 2D**). The absence
334 of significant changes in E2-induced targets, such as *Lif*, *Mcm2*, *Ccnd1*, and *Fgf18*, at 4 dpc
335 (**Fig. 2E**) supports our conclusion that ATG14 is required for P4-mediated but not for E2-
336 mediated actions during uterine receptivity. Moreover, the normal serum levels of E2 and P4

337 at D4 of pregnancy rule out any hormonal imbalances, strongly suggesting that the observed
338 phenotype is primarily due to the uterine-specific loss of *Atg14* (**Fig. 2F**).

339 ***Atg14* is required for maintaining oviductal cell structural integrity and embryo**
340 **transport**

341 Given that *Atg14* cKO mice had impaired embryo implantation, we wondered whether
342 embryos are reaching the uterus timely through the oviduct. To determine this, we flushed
343 embryos from both the control and cKO mice uteri on day 4 of pregnancy. Interestingly, in cKO
344 mice, we could retrieve only 1-2% of embryos from their uteri, whereas in control mice, 100%
345 of well-developed blastocysts were retrieved from their uteri (**Fig. 3A & B**). To ensure the
346 timely transport of all embryos from the oviducts to the uteri, we also flushed oviducts from
347 both control and cKO mice. As expected, in the control mice oviduct flushing, we could not
348 recover any embryos or blastocysts, indicating their precise and timely transport to the uterus.
349 Unexpectedly, oviduct flushing from cKO mice resulted in the retrieval of approximately 80-
350 90% of blastocysts, suggesting their potential entrapment within the oviducts, impeding their
351 transit to the uterus (**Fig. 3A & B)**. At 4 dpc, there was no significant difference in the average
352 number of blastocysts, morula, or non-viable or retrieved from *Atg14* control uteri and cKO
353 oviducts (**Fig. S4A).** However, we noted that the percentage of developmentally delayed
354 embryos appeared to be higher in *Atg14* cKO oviducts compared to the embryos retrieved
355 from control uteri (**Fig. 3C**). The histological analysis further confirmed an entrapped embryo
356 in the ampulla of *Atg14* cKO at 4 dpc as shown in **Fig. 3D**. Given the embryo retention
357 phenotype in oviduct, we sought to determine if ATG14 is expressed in this region. Consistent
358 with previous studies reporting PR-cre activity in the isthmus [8, 29], we found a significant
359 depletion of ATG14 in the isthmus compared to the ampulla (**Fig. S2A**). Further, the increased
360 p62 and LC3B expression in cKO oviducts suggests that the observed embryo retention
361 phenotype might be attributed to the loss of ATG14-dependent autophagy in cKO oviducts
362 (**Fig. S2B**).

363 Similarly, when we super-ovulated the mice and looked for the embryos on day 4 of
364 pregnancy, we could recover ~20-25 embryos from the cKO mice oviducts compared to only
365 4-5 embryos that were able to reach the uterus. In comparison, in control mice, 90% of
366 embryos were able to complete their pre-destined and timely transport to the uterus (**Fig. 3E**),
367 except 1-2% of unfertilized embryos, which remained in their oviducts.

368 To understand the underlying cause for retained embryos in cKO mice oviducts, we
369 performed histology analysis and determined the structural morphology of their oviducts. The
370 cKO mice oviduct lining shows marked eosinophilic cytoplasmic change akin to
371 decidualization in human oviducts. Some of the cells showed degenerative changes with
372 cytoplasmic vacuolization and nuclear pyknosis, loss of nuclear polarity, and loss of distinct
373 cell borders giving an appearance of fusion of cells (**Fig. 3F**). The marked cytologic
374 enlargement appears to cause luminal obliteration or narrowing resulting in a completely
375 unorganized, obstructed, and narrow lumen, thereby, hampering the path of embryos to reach
376 the uterus as evident from an entrapped embryo shown in **Fig. 3D**. Further, epithelial
377 (cytokeratin KRT8-positive) and myosalpinx (α-smooth muscle active [SMA]-positive,) marker
378 analysis revealed completely distorted epithelial structures (in terms of loss of epithelial cell
379 integrity) with no overt defects in the muscle organization in oviducts of cKO mice (**Fig. 3F,**
380 **lower panel**). Notably, the ampullary region from cKO oviducts seems to be normal with intact
381 epithelial and smooth muscle structures as evident from KRT8 and SMA staining (**Fig. 3F,**
382 **upper panel**).

383 **Selective loss of *Atg14* in oviduct cilia is dispensable for female fertility**

384 The oviduct epithelium primarily consists of two types of cells: ciliated and secretory
385 (non-ciliated) cells. Ciliated cells play a role in embryo and oocyte transport by means of ciliary
386 beat, and non-ciliated/secretory cells produce an oviductal fluid that is rich in amino acids and
387 various molecules, thereby providing an optimal micro-environment for sperm capacitation,
388 fertilization, embryonic survival, and development [36]. Therefore, we determined whether
389 oviducts from cKO mice possess normal ciliated and secretory cell composition. To do so, we

390 examined the expression of various markers, including acetylated-α-tubulin (cilia marker),
391 FOXJ1 (ciliogenesis markers), and PAX8 (non-ciliated/ secretory cell marker) in control and
392 cKO oviducts. As shown in **Fig. 4A,** while we observed normal ciliary structures in the ampulla
393 of both control and cKO oviducts, there was a substantial loss of the ciliary epithelial cells
394 (indicated by fewer α-tubulin and FOXJ1-positive cells) **(Fig. 4B, left panel and Fig. S3**) as
395 well as secretory cells (indicated by fewer PAX-8 positive cells) in the isthmus of cKO oviducts
396 (**Fig. 4B, right panel)**.

397 Given the importance of cilia in embryo transport, we wondered whether the loss of
398 *Atg14* in oviduct cilia has any impact on embryo transport. To address this, we generated a
399 *Foxj1*-cre/+; *Atg14* f/f mouse model, wherein *Atg14* will be ablated only in ciliary epithelial
400 cells. We observed that ciliated epithelial cells that were positive for acetylated α-tubulin
401 staining did not appear to be different in Foxj1$^{Cre/+;}$ *Atg14* f/f mice oviduct compared to controls
402 suggesting normal ciliogenesis in Foxj1$^{Cre/+}$; *Atg14* f/f mice (**Fig. 4C**).

403 The 6-month breeding trial revealed that loss of *Atg14* in oviductal cilia had no impact
404 on fertility (**Table 2**, **Fig. 4D & E**). Consistently, D5 implantation study analysis showed ~7-8
405 visible embryo implantation sites in *Foxj1/Atg14* cKO mice like their corresponding controls
406 suggesting that embryos were able to make their way to the uterus in a timely manner and
407 undergo implantation despite the ablation of *Atg14* in the oviduct ciliary epithelial cells (**Fig.**
408 **4F**). These findings suggest that ciliary expression of *Atg14* is dispensable for embryo
409 transport.

410 **ATG14 maintains mitochondria integrity and prevents unscheduled pyroptosis**
411 **activation in the oviduct to enable embryo transport**

412 To gain more insights into structural defects, we performed TEM analysis on oviducts
413 collected from both control and cKO females on day 4 of pregnancy. Interestingly, oviducts
414 from cKO females had numerous altered mitochondrial structures with abnormally enlarged
415 mitochondria and a less dense matrix compared to control oviducts that had small and
416 compact mitochondria with tight cristae and a dense matrix (**Fig. 5A**). Corroborating and

417 extending those findings, we observed marked reductions of mitochondria network (as defined
418 by TOMM20 staining) in the sub-nuclear region of oviducts from *Atg14* cKO mice compared
419 to more densely packed mitochondrial network in the sub-nuclear region of control ones (**Fig.**
420 **5B**). Further co-localization study analysis revealed a uniform co-localization of Cytochrome
421 C with the TOM20 positive mitochondrial network in control oviducts reflecting the intact
422 mitochondrial integrity (**Fig. 5B**). In contrast, in *Atg14* cKO oviducts, cells with disrupted
423 mitochondrial networks exhibited increased cytosolic leakage of Cytochrome C (**Fig. 5B**).
424 Additionally, analysis of various mitochondrial functional and architecture markers (*Cox4i2*,
425 *Pink1*, *Opa1,* and *Drp1* showed reduced expression in *Atg14* cKO compared to controls (**Fig.**
426 **5C**).

427 Having identified the cellular mechanisms of Atg14, we aimed to delineate the
428 underlying molecular mechanisms associated with Atg14 function in the oviduct. Since we
429 found mitochondrial defects with ATG14 loss and altered mitochondrial structures have been
430 linked to the activation of pyroptosis, we determined if ATG14 regulates pyroptosis in oviduct
431 [37-39]. First, we assessed the key primary executors of the pyroptosis pathway, Gasdermin
432 D (GSDMD), and caspase-1. Immunofluorescence analysis revealed a remarkable
433 upregulation in GSDMD and caspase-1 expression in the cKO oviducts compared to controls
434 (**Fig. 5D & E**). However, histological analysis of uterus and ovary showed no induction in
435 GSDMD expression compared to their corresponding controls (**Fig. 5F**). Western blot analysis
436 further confirmed elevated expression of caspase-1 and GSDMD in cKO oviducts in
437 comparison to control oviducts as shown in **Fig. 5G.** Additionally, the qPCR analysis
438 demonstrated elevated levels of inflammatory markers, such as *Tnf-α* and *Cxcr3* in cKO
439 oviducts compared to control ones (**Fig. 5H**). Based on these findings, we posit that Atg14
440 plays a crucial role in regulating the pyroptotic pathway by preserving the mitochondrial
441 structural and functional integrity, and activation of pyroptosis owing to loss of ATG14 within
442 the oviduct.

443 To substantiate the notion, we also evaluated the impact of unscheduled activation of
444 pyroptosis on embryo transport. To test this, we employed a pyroptosis inducer, Polyphyllin
445 VI, and chose the optimal dose based on the established studies [34]. Wild-type females were
446 mated with virile males and following the plug detection treated with Polyphyllin VI for three
447 consecutive days from 1 to 4 dpc (**Fig. 5E**). We chose to treat to 1 to 4 dpc for treatment to
448 activate unwarranted pyroptosis in oviduct during the embryo transport. Following the
449 treatments, the oviducts, and uteri from both vehicle-treated and Polyphyllin VI-treated were
450 flushed. We found that pregnant females treated with Polyphyllin VI showed ~50% embryo
451 retention in the oviduct, whereas in the vehicle-treated group, no embryos were retained in
452 the oviduct (**Fig. 6A-C**). Further analysis of embryos retrieved from Polyphyllin-treated
453 oviducts showed more percentage of developmentally delayed and non-viable embryos
454 compared to embryos recovered from control uteri (**Fig. 6D**). The average number of embryos
455 recovered from polyphyllin- and vehicle-treated mice was not significantly different (**Fig. S4B**).
456 Histological analysis showed a marked induction in GSDMD expression compared to vehicle-
457 treated mice oviducts (**Fig. 6E**). However, precisely activating the unscheduled pyroptosis
458 during the critical period of embryo transport is technically challenging. Nonetheless, our
459 findings provide evidence that unscheduled pyroptosis adversely affects embryo transport
460 through the oviduct. Taken together, these results demonstrate that *Atg14* safeguards
461 pyroptosis activation in the oviduct and allows the smooth transport of embryos to the uterus
462 (**Fig. 6F**).

463 **Discussion**

464 In this study, we delineated the essential role of ATG14 in maintaining the structural
465 integrity of the oviduct by preventing pyroptosis, which enables smooth embryo transit during
466 early pregnancy. Specifically, we dissected the tissue-specific functions of ATG14 in the FRT
467 using Cre driver mice targeting the female reproductive tract. Given that PR-Cre expresses
468 postnatally in different tissues of FRT such as corpus luteum, oviducts, and different cellular
469 compartments (epithelial, stromal, and myometrium) of uteri [29], we found that conditional
470 ablation of ATG14-mediated functions in FRT resulted in infertility owing to hampered
471 transport of embryos from the oviduct. Additionally, *Atg14* loss in uteri causes impaired embryo
472 implantation and receptivity. Its ablation in the oviduct might lead to the activation of
473 pyroptosis, an inflammatory-associated apoptosis pathway that causes the retention of
474 embryos in the oviduct and prevents their timely transport to the uterus. However, the ovarian-
475 specific functions were found to be unaffected despite the loss of *Atg14* in the corpus luteum.

476 The human endometrium is a complex dynamic tissue that undergoes sequential
477 phases of proliferation and differentiation to support embryo implantation during the
478 conceptive. However, in the absence of an implanting embryo, the endometrium sheds
479 (menstruation) and initiates the regeneration process [40]. Previous reports indicated that
480 autophagy is modulated in the human endometrium during the menstrual cycle. For example,
481 autophagy is altered during the proliferative and secretory phases of the menstrual cycle with
482 its highest activity occurring during the secretory phase when the stroma is decidualized [41].
483 Similarly, the level of autophagy was higher in postmenopausal human uterine epithelial cells
484 compared to premenopausal uterine epithelial cells indicating the onset of autophagy upon
485 estrogen deprivation [42]. Although all these studies reported that autophagy is hormonally
486 regulated, however, the role of autophagy-specific proteins in the endometrium was not
487 established till our group's recent reports. Specifically, studies from our group reported the
488 role of three different autophagy-associated proteins: FIP200 [25], ATG16L [27], and BECLIN-
489 1 in uterine functions [26]. Conditional ablation of *Fip200* and *Atg16l* in the uterus displayed
490 fertility defects owing to impaired implantation, uterine receptivity, and decidualization defects.

491 On the contrary, loss of *Beclin1* in the uterus caused progressive loss of endometrial
492 progenitor stem cells resulting in severe uterine developmental defects and rendering the mice
493 infertile [26]. Although the autophagy-related proteins we studied so far influenced uterine
494 functions, [25-27], we found a distinct role for ATG14 in both the uterine and oviduct-specific
495 functions. It is intriguing to note that the absence of ATG14 did not affect the tissue integrity
496 of the uterus. However, the severe structural abnormalities in the oviduct due to *Atg14* ablation
497 unearthed a unique function of Atg14 in maintaining oviduct homeostasis. This distinctive role
498 of ATG14, unlike other autophagy proteins, might be due to its pivotal role in the assembly of
499 PtdIns3K complexes which is not the case for either FIP200 or ATG16L [40, 43, 44].
500 Nevertheless, understanding the specific contributions of each core autophagy protein in
501 reproductive tract functions is necessary which requires substantial efforts.

502 The retention of preimplantation embryos in the oviduct has been established as a
503 significant contributor to implantation failures, presenting challenges to the overall
504 reproductive health of women [8-10]. Embryo transport in the oviduct is known to be controlled
505 primarily by two major physiological responses: ciliary activity and muscle contractility. In our
506 study, a dramatic decrease in the number of Foxj1^{+ve} ciliary epithelial cells and Pax-8^{+ve}
507 secretory cells in *Atg14* cKO mice implied cell-type specific actions for ATG14 in the oviduct.
508 Interestingly, the specific ablation of *Atg14* in Foxj1+ve ciliary epithelial cells of the oviduct
509 does not appear to impact fertility. This suggests that the absence of ATG14 within ciliary cells
510 does not impact the process of embryo transport. Although unexpected, this is consistent with
511 other reports that have demonstrated the dispensability of cilia for embryo transport in the
512 oviduct [8, 9].

513 Pyroptosis is a highly inflammatory form of programmed cell death, characterized by
514 cell swelling, flattening of the cytoplasm, and large bubbles-like protrusions on the plasma
515 membrane [45-47]. Several recent studies found a link between autophagy and pyroptosis
516 [48]. *In vivo* studies also found that mice lacking the autophagy genes *Atg14*, *Fip200*, *Atg5*, or
517 *Atg7* in myeloid cells had more pronounced lung inflammation [49]. In our study, cellular
518 swelling, and fused membranous structures (a unique feature of activation of pyroptosis)

519 observed in the oviductal epithelial folds from *Atg14* cKO mice. This aberrant activation of the
520 pyroptosis pathway due to loss of *Atg14* appears to adversely affect the oviduct cellular
521 structural integrity. These findings have implications beyond the oviduct, as autophagy can
522 modulate the inflammatory signaling pathway through different avenues. For example, first,
523 autophagy prevents mitochondrial reactive oxygen species release that can activate the
524 inflammasome by inhibiting IL1-β and IL18 production through the digestion of dysfunctional
525 mitochondria [50]. Second, autophagy is capable of targeting inflammasome complexes for
526 degradation, which prevents the cleavage of pro-IL-1β and pro-IL-18 into biologically active
527 forms. Finally, autophagy machinery further regulates IL-1β levels by engulfing and degrading
528 pro-IL-1β proteins [50]. In our study, accumulation of abnormally enlarged and dysfunctional
529 mitochondria in the absence of ATG14 in the oviduct clearly suggests the induction of severe
530 inflammatory conditions hampering the embryo transit through the oviduct. These findings are
531 further substantiated by the upregulation of pivotal mediators of the pyroptosis program,
532 including GSDMD and caspase-1, in *Atg14* cKO mice. Notably, the induction of pyroptosis in
533 the absence of ATG14 is specifically localized to the oviducts, with no parallel activation
534 detected in either the ovary or uterus. One potential reason for this observed phenomenon
535 could be the oviduct's unique molecular signatures that get activated in response to the
536 presence of gametes. A recent study by Finnerty et al. (2024) reported that sperm induce pro-
537 inflammatory conditions in the oviduct, which are preceded by an anti-inflammatory response
538 triggered by the presence of embryos [51]. The persistent activation of inflammatory or
539 pyroptotic conditions following the loss of Atg14 suggests that Atg14 may be a critical
540 autophagy protein responsible for suppressing pyroptosis in the oviduct. Moreover,
541 understanding the complex rheostat between the ATG14 and inflammation regulatory axis is
542 highly intriguing and will necessitate future studies employing sophisticated models, such as
543 combined knockout mice where ATG14 is deleted alongside key inflammatory regulators (e.g.,
544 NLRP3, GSDMD, or CASPASE-1).

545 In this report, we revealed tissue-specific roles of ATG14 in governing oviductal
546 transport, and uterine receptivity which are necessary for embryo implantation and pregnancy

547 establishment. Of mechanistic insights, we delineated a novel function of ATG14 as a negative
548 regulator of pyroptosis, which is vital for proper embryo transport in the oviduct (**Fig. 6F**). Thus,
549 this study not only sheds light on the involvement of autophagy in oviductal embryo transport
550 but also underscores the importance of autophagy in preserving the oviduct tissue integrity.
551 Such insights hold promise for advancing our understanding of gynecological pathologies
552 associated with the oviduct including tubal pregnancies.

553 **Acknowledgments**

554 We thank Goutham Davuluri, and Ashirbad Guria from our group for the technical assistance.
555 We thank Dr. Robert Lawrence (senior editor at Baylor College of Medicine) for assistance
556 with manuscript editing. We thank WashU Molecular Microbiology Imaging Facility for
557 assisting us with transmission electron microscopy. This work was funded, in part, by the
558 National Institutes of Health/National Institute of Child Health and Human Development
559 (grants R01HD102680, R01HD104813, and R01HD065435) to RK, R01 HD-042311 to JPL,
560 and in part by National Institutes of Health/National Heart, Lung, and Blood Institute (grant
561 R35HL145242) to MJH.

562 **Authors' roles**

563 PP and RK designed experiments, conducted most of the studies, analyzed the data, and
564 wrote the manuscript. AKO, VKM, and MNR, conducted some of the experiments. MJH, JL,
565 SA, YZ, and KHM, provided critical reagents for the study. RM helped us with oviduct
566 pathology phenotype analysis. RK conceived the project, supervised the work, and wrote the
567 manuscript. All authors critically reviewed the manuscript.

568 **Conflict of Interest**

569 The authors have declared that no conflict of interest exists.

570 **Table 1**: **Six-month breeding trial of *Atg14* control and cKO females with wild-type males**

571 **Table 2**: **Six-month breeding trial of *Foxj1*/*Atg14* control and cKO females with wild-type**

572 **males**

573

574 **Figure legends**

575 **Figure 1: *Atg14* loss in the FRT results in infertility.** (**A**) Representative immunofluorescent
576 images of uteri from pregnant mice (n=3) at the indicated days of pregnancy stained with an
577 ATG14-specific antibody (green). LE: luminal epithelium, G: glands, S: stroma, Scale bar: 100
578 µm. Rabbit IgG was used as an isotype control for staining. (**B**) Relative transcript levels of
579 *Atg14* mRNA in uteri from pregnant mice (n=3-5) at indicated days of pregnancy. mRNA levels
580 are normalized to levels of 18S m-RNA. Data are presented as mean ±SEM; **P<0.01,
581 P>0.05, ns=non-significant. (**C**) Relative mRNA levels of *Atg14* in 8-week-old virgin control
582 and cKO mice uteri, ovary, and liver (n=5). mRNA levels are normalized to levels of 18S
583 mRNA. Data are presented as mean ±SEM; ***P<0.001, P>0.05, ns=non-significant. (**D**)
584 Representative immunofluorescent images of ATG14 expression in different uterine
585 compartments in control (n=5) and *Atg14* cKO mice (n=5). LE: luminal epithelium, G: glands,
586 S: stroma. (**E**) (*left panel*) Relative number of pups/female/litter and (*right panel*) and relative
587 number of total pups/months of *Atg14* control (n=4) and cKO mice (n=5) sacrificed after the
588 breeding trial. Data are presented as mean ±SEM; ***P<0.001; P>0.05, ns=non-significant.

589 **Figure 2: *Atg14* is critical for embryo implantation, and uterine receptivity.** (**A**) Gross
590 images of 5.0 dpc uteri of control (n=5) and *Atg14* cKO mice (n=5) injected with Chicago Sky
591 Blue dye to visualize implantation sites (denoted by black arrows) (*left panel*). H&E-stained
592 cross-sections (4X & 40X) of 5.0 dpc uteri of control (n=5) and *Atg14* cKO (n=5) mice to
593 visualize embryo implantation (*Middle panel*). The asterisk denotes the embryo.
594 Immunofluorescence analysis of uterine tissues from control (n=5) and *Atg14* cKO mice (n=5),
595 stained with MUC1 and KRT8 (*right panel*). LE: luminal epithelium, G: glands, S: stroma. (**B**)
596 Representative immunofluorescence images of uteri from control (n=5) and *Atg14* cKO mice
597 (n=5) stained for Ki-67 following Oil or E2 or E2+P4 treatment (n=5 mice/group); scale bar:
598 100 µm. LE: luminal epithelium, G: glands, S: stroma. (**C**) Immunofluorescence analysis of
599 KRT8 (green), MUC1 (Red), and (**D**) Ki-67 (red) in the uteri of 4 dpc control and *Atg14* cKO
600 mice; scale bars, 100 µm. (**E**) Relative transcript levels of *Lif*, *Mcm2*, *Ccnd1,* and *Fgf18* in

601 control and cKO uteri at 4dpc. mRNA levels are normalized to levels of 18S m-RNA. Data are
602 presented as mean ±SEM; ns=non-significant. (**F**) Levels of steroid hormones estradiol and
603 progesterone from serum collected during euthanasia of 4 dpc control or cKO mice.

604 **Figure 3: *Atg14* is critical for embryo transport in oviduct.** (**A**) Representative images
605 (*upper panel*) and (**B**) Percentage of embryos (*lower panel*) collected at 4 dpc from the uteri
606 or the oviducts of control (n=6) or *Atg14* cKO mice (n=6-8). (**C**) Percentage of blastocysts,
607 morulae, developmentally delayed or nonviable embryos collected from *Atg14* control mice
608 uteri and Atg14 cKO mice oviducts at 4 dpc. (**D**) Histological analysis using H&E staining of
609 the ampullary and isthmic region of the oviduct from control and *Atg14* cKO female mice at 4
610 dpc (n=3 mice/genotype). (**E**) Embryos retrieved from the oviduct and uterus of super-ovulated
611 *Atg14* control or cKO mice at 4 dpc (n=3 mice/genotype). (**F**) Immunofluorescence analysis of
612 KRT8 (green), and α-SMA (Red), in the oviduct of 4 dpc control (n=5) and *Atg14* cKO mice
613 (n=5) ampulla (*upper panel*) and isthmus (*lower panel*).

614 **Figure 4: *Atg14* loss in oviduct cilia is dispensable for embryo transport. (A)**
615 Immunofluorescence analysis of acetylated α-tubulin (green), and DAPI (blue) in oviduct of 4
616 dpc control (n=5) and *Atg14* cKO mice (n=5). (**B**) Immunohistochemical analysis of FOXJ1
617 and PAX8 at 4 dpc (n=5). (**C**) Immunohistochemical analysis of acetylated α-tubulin in 8-week-
618 old control (n=5) and *Foxj1*/*Atg14* cKO mice (n=5). Images are taken at 6X and 40X. Scale
619 bar: 100μm and 10 μm. (**D & E**) Relative number of pups/females/litter and relative number
620 of total pups/months of control (n=5) and *Foxj1*/*Atg14* cKO mice (n=5) sacrificed after the
621 breeding trial. Data are presented as mean ± SEM; P>0.05, ns=non-significant. (**F**) Gross
622 images of 5.0 dpc uteri of control (n=3) and *Foxj1/Atg14 cKO mice* (n=3) injected with Chicago
623 Sky Blue dye to visualize implantation sites (denoted by black arrows).

624 **Figure 5: ATG14 facilitates embryo transport in the oviduct by preserving mitochondrial**
625 **integrity and inhibiting the activation of pyroptosis**. (**A**) Transmission electron microscopy
626 of oviducts at 4 dpc from control (n=3) and *Atg14* cKO (n=3)**.** Black arrowheads in control
627 oviducts show small, compact mitochondria with tight cristae. Red arrowheads in cKO oviducts

628 show abnormally enlarged mitochondria with loose cristae. (**B**) Immunofluorescence analysis
629 of TOM20 (green) and Cytochrome C (red) in *Atg14* control and cKO oviducts cryo-sections.
630 The inset shows the zoomed image of the selected area from control and cKO oviducts,
631 Arrowheads in cKO inset oviduct section show the leaked cytochrome C in the cytoplasm.
632 Tissues were counterstained with DAPI (blue) to visualize nuclei; scale bars, 10 μm. (**C**)
633 Relative transcript levels of *Opa1*, *Cox4i2*, *Drp1,* and Pink1 in oviduct tissues. Data are
634 presented as mean ±SEM. *P<0.05; **P<0.01 compared with controls. 18S was used as an
635 internal control (**D**) Immunofluorescence analysis of GSDMD (red) + KRT8 (green), Caspase-
636 1 (red) + KRT8 (green) in oviducts of adult control (n=5), and *Atg14* cKO mice (n=5). Tissues
637 were counterstained with DAPI (blue) to visualize nuclei; scale bars, 100 μm. (**E**)
638 Immunohistochemical analysis of GSDMD expression in adult oviduct tissues (*left panel*). The
639 middle and -right panels show the zoom-in images to show the relative GSDMD expression in
640 the ampulla and isthmus section from control and cKO oviducts. (**F**) Immunohistochemical
641 analysis of GSDMD expression in adult uterus and ovary tissues (**G**) Western blotting to show
642 protein levels of Caspase-1, and GSDMD in oviduct tissues. β-actin is used as a loading
643 control. (**H**) Relative transcript levels of *Tnf-α* and *Cxcr3* in oviduct tissues. Data are presented
644 as mean ±SEM. *P<0.05; **P<0.01; ***P<0.001 compared with controls. 18S was used as an
645 internal control.

646 **Figure 6: Pharmacological activation of pyroptosis in the oviduct inhibits embryo**
647 **transport.** (**A**) Experimental strategy for pyroptosis activation in pregnant female mice (**B**)
648 Embryos flushed from the vehicle (n=3) or polyphyllin VI treated (n=3) D-4 pregnant females.
649 (**C**) Percentage of embryos recovered from oviducts or uteri. (**D**) Percentage of blastocysts,
650 morulae, developmentally delayed or nonviable embryos collected from vehicle or Polyphyllin
651 IV oviducts at 4 dpc. (**E**) Immunohistochemistry to show GSDMD expression in the isthmus
652 section of polyphyllin IV-treated and vehicle-treated mice. 40X objective, Scale bar: 5 μm. (**F**)
653 Graphical illustration to show embryo transport and pyroptosis regulation in the oviduct.

654 **References**

655

656 1. Wang, H. and S.K. Dey, *Roadmap to embryo implantation: clues from mouse models.* Nat Rev
657 Genet, 2006. **7**(3): p. 185-99.
658 2. Ford, M.J., et al., *Oviduct epithelial cells constitute two developmentally distinct lineages that*
659 *are spatially separated along the distal-proximal axis.* Cell Rep, 2021. **36**(10): p. 109677.
660 3. McKey, J., et al., *Integration of mouse ovary morphogenesis with developmental dynamics of*
661 *the oviduct, ovarian ligaments, and rete ovarii.* Elife, 2022. **11**.
662 4. Harwalkar, K., et al., *Anatomical and cellular heterogeneity in the mouse oviduct-its potential*
663 *roles in reproduction and preimplantation developmentdagger.* Biol Reprod, 2021. **104**(6): p.
664 1249-1261.
665 5. Dirksen, E.R. and P. Satir, *Ciliary activity in the mouse oviduct as studied by transmission and*
666 *scanning electron microscopy.* Tissue Cell, 1972. **4**(3): p. 389-403.
667 6. Li, S., et al., *Estrogen receptor alpha is required for oviductal transport of embryos.* FASEB J,
668 2017. **31**(4): p. 1595-1607.
669 7. Jiang, R., et al., *CDC42 governs normal oviduct multiciliogenesis through activating AKT to*
670 *ensure timely embryo transport.* Cell Death Dis, 2022. **13**(9): p. 757.
671 8. Herrera, G.G.B., et al., *Oviductal Retention of Embryos in Female Mice Lacking Estrogen*
672 *Receptor alpha in the Isthmus and the Uterus.* Endocrinology, 2020. **161**(2).
673 9. Wang, H., et al., *Aberrant cannabinoid signaling impairs oviductal transport of embryos.* Nat
674 Med, 2004. **10**(10): p. 1074-80.
675 10. Qian, J., et al., *Caffeine consumption during early pregnancy impairs oviductal embryo*
676 *transport, embryonic development and uterine receptivity in mice.* Biol Reprod, 2018. **99**(6): p.
677 1266-1275.
678 11. Klionsky, D.J., *Autophagy: from phenomenology to molecular understanding in less than a*
679 *decade.* Nat Rev Mol Cell Biol, 2007. **8**(11): p. 931-7.
680 12. Wen, X. and D.J. Klionsky, *An overview of macroautophagy in yeast.* J Mol Biol, 2016. **428**(9 Pt
681 A): p. 1681-99.
682 13. Itakura, E., et al., *Beclin 1 forms two distinct phosphatidylinositol 3-kinase complexes with*
683 *mammalian Atg14 and UVRAG.* Mol Biol Cell, 2008. **19**(12): p. 5360-72.
684 14. Sun, Q., et al., *Identification of Barkor as a mammalian autophagy-specific factor for Beclin 1*
685 *and class III phosphatidylinositol 3-kinase.* Proc Natl Acad Sci U S A, 2008. **105**(49): p. 19211-
686 6.
687 15. Wang, Y.Y., X.L. Liu, and R. Zhao, *Induction of Pyroptosis and Its Implications in Cancer*
688 *Management.* Front Oncol, 2019. **9**: p. 971.
689 16. Man, S.M., R. Karki, and T.D. Kanneganti, *Molecular mechanisms and functions of pyroptosis,*
690 *inflammatory caspases and inflammasomes in infectious diseases.* Immunol Rev, 2017. **277**(1):
691 p. 61-75.
692 17. Wei, X., et al., *Role of pyroptosis in inflammation and cancer.* Cell Mol Immunol, 2022. **19**(9):
693 p. 971-992.
694 18. Lin, L., et al., *Autophagy, Pyroptosis, and Ferroptosis: New Regulatory Mechanisms for*
695 *Atherosclerosis.* Front Cell Dev Biol, 2021. **9**: p. 809955.
696 19. Li, X., et al., *Autophagy, Pyroptosis and Ferroptosis are Rising Stars in the Pathogenesis of*
697 *Diabetic Nephropathy.* Diabetes Metab Syndr Obes, 2024. **17**: p. 1289-1299.
698 20. Zhao, H., et al., *The Role of Autophagy and Pyroptosis in Liver Disorders.* Int J Mol Sci, 2022.
699 **23**(11).
700 21. Kong, Y., et al., *The Natural Flavonoid Galangin Elicits Apoptosis, Pyroptosis, and Autophagy*
701 *in Glioblastoma.* Front Oncol, 2019. **9**: p. 942.
702 22. Kim, J.Y., et al., *Streptococcus pneumoniae induces pyroptosis through the regulation of*
703 *autophagy in murine microglia.* Oncotarget, 2015. **6**(42): p. 44161-78.

704 23. Song, Z.H., et al., *Germ cell-specific Atg7 knockout results in primary ovarian insufficiency in*
705 *female mice.* Cell Death Dis, 2015. **6**(1): p. e1589.
706 24. Gawriluk, T.R., et al., *Beclin-1 deficiency in the murine ovary results in the reduction of*
707 *progesterone production to promote preterm labor.* Proc Natl Acad Sci U S A, 2014. **111**(40):
708 p. E4194-203.
709 25. Oestreich, A.K., et al., *The autophagy protein, FIP200 (RB1CC1) mediates progesterone*
710 *responses governing uterine receptivity and decidualizationdagger.* Biol Reprod, 2020. **102**(4):
711 p. 843-851.
712 26. Popli, P., et al., *Beclin-1-dependent autophagy, but not apoptosis, is critical for stem-cell-*
713 *mediated endometrial programming and the establishment of pregnancy.* Dev Cell, 2023.
714 **58**(10): p. 885-897 e4.
715 27. Oestreich, A.K., et al., *The Autophagy Gene Atg16L1 is Necessary for Endometrial*
716 *Decidualization.* Endocrinology, 2020. **161**(1).
717 28. Matsunaga, K., et al., *Two Beclin 1-binding proteins, Atg14L and Rubicon, reciprocally regulate*
718 *autophagy at different stages.* Nat Cell Biol, 2009. **11**(4): p. 385-96.
719 29. Soyal, S.M., et al., *Cre-mediated recombination in cell lineages that express the progesterone*
720 *receptor.* Genesis, 2005. **41**(2): p. 58-66.
721 30. Zhang, Y., et al., *A transgenic FOXJ1-Cre system for gene inactivation in ciliated epithelial cells.*
722 Am J Respir Cell Mol Biol, 2007. **36**(5): p. 515-9.
723 31. Chadchan, S.B., et al., *Antibiotic therapy with metronidazole reduces endometriosis disease*
724 *progression in mice: a potential role for gut microbiota.* Hum Reprod, 2019. **34**(6): p. 1106-
725 1116.
726 32. Chojnacki, A.K., et al., *Tissue imaging reveals disruption of epithelial mitochondrial networks*
727 *and loss of mitochondria-associated cytochrome-C in inflamed human and murine colon.*
728 Mitochondrion, 2023. **68**: p. 44-59.
729 33. Kommagani, R., et al., *The Promyelocytic Leukemia Zinc Finger Transcription Factor Is Critical*
730 *for Human Endometrial Stromal Cell Decidualization.* PLoS Genet, 2016. **12**(4): p. e1005937.
731 34. Teng, J.F., et al., *Polyphyllin VI Induces Caspase-1-Mediated Pyroptosis via the Induction of*
732 *ROS/NF-kappaB/NLRP3/GSDMD Signal Axis in Non-Small Cell Lung Cancer.* Cancers (Basel),
733 2020. **12**(1).
734 35. Tong, W. and J.W. Pollard, *Progesterone inhibits estrogen-induced cyclin D1 and cdk4 nuclear*
735 *translocation, cyclin E- and cyclin A-cdk2 kinase activation, and cell proliferation in uterine*
736 *epithelial cells in mice.* Mol Cell Biol, 1999. **19**(3): p. 2251-64.
737 36. Ito, S., Y. Yamamoto, and K. Kimura, *Analysis of ciliogenesis process in the bovine oviduct based*
738 *on immunohistochemical classification.* Mol Biol Rep, 2020. **47**(2): p. 1003-1012.
739 37. Liu, Q., et al., *The role of mitochondria in NLRP3 inflammasome activation.* Mol Immunol,
740 2018. **103**: p. 115-124.
741 38. Shi, Y., et al., *Echinacoside Induces Mitochondria-Mediated Pyroptosis through Raf/MEK/ERK*
742 *Signaling in Non-Small Cell Lung Cancer Cells.* J Immunol Res, 2022. **2022**: p. 3351268.
743 39. Wang, Y., et al., *Mitochondrial ROS promote macrophage pyroptosis by inducing GSDMD*
744 *oxidation.* J Mol Cell Biol, 2019. **11**(12): p. 1069-1082.
745 40. Popli, P., A.J. Sun, and R. Kommagani, *The Multifaceted Role of Autophagy in Endometrium*
746 *Homeostasis and Disease.* Reprod Sci, 2022. **29**(4): p. 1054-1067.
747 41. Choi, J., et al., *Differential induction of autophagy by mTOR is associated with abnormal*
748 *apoptosis in ovarian endometriotic cysts.* Mol Hum Reprod, 2014. **20**(4): p. 309-17.
749 42. Zhou, S., et al., *Author Correction: Menopause-induced uterine epithelium atrophy results from*
750 *arachidonic acid/prostaglandin E2 axis inhibition-mediated autophagic cell death.* Sci Rep,
751 2020. **10**(1): p. 6915.
752 43. Fan, W., A. Nassiri, and Q. Zhong, *Autophagosome targeting and membrane curvature sensing*
753 *by Barkor/Atg14(L).* Proc Natl Acad Sci U S A, 2011. **108**(19): p. 7769-74.

754 44. Diao, J., et al., *ATG14 promotes membrane tethering and fusion of autophagosomes to*
755 *endolysosomes.* Nature, 2015. **520**(7548): p. 563-6.
756 45. Ma, X., et al., *LPS Mediates Bovine Endometrial Epithelial Cell Pyroptosis Directly Through Both*
757 *NLRP3 Classical and Non-Classical Inflammasome Pathways.* Front Immunol, 2021. **12**: p.
758 676088.
759 46. Cookson, B.T. and M.A. Brennan, *Pro-inflammatory programmed cell death.* Trends Microbiol,
760 2001. **9**(3): p. 113-4.
761 47. Jorgensen, I. and E.A. Miao, *Pyroptotic cell death defends against intracellular pathogens.*
762 Immunol Rev, 2015. **265**(1): p. 130-42.
763 48. Liu, J., et al., *Autophagy blockage promotes the pyroptosis of ox-LDL-treated macrophages by*
764 *modulating the p62/Nrf2/ARE axis.* J Physiol Biochem, 2021. **77**(3): p. 419-429.
765 49. Lu, Q., et al., *Homeostatic Control of Innate Lung Inflammation by Vici Syndrome Gene Epg5*
766 *and Additional Autophagy Genes Promotes Influenza Pathogenesis.* Cell Host Microbe, 2016.
767 **19**(1): p. 102-13.
768 50. Netea-Maier, R.T., et al., *Modulation of inflammation by autophagy: Consequences for human*
769 *disease.* Autophagy, 2016. **12**(2): p. 245-60.
770 51. Finnerty, R.M., et al., *Multi-omics analyses and machine learning prediction of oviductal*
771 *responses in the presence of gametes and embryos.* bioRxiv, 2024.

772

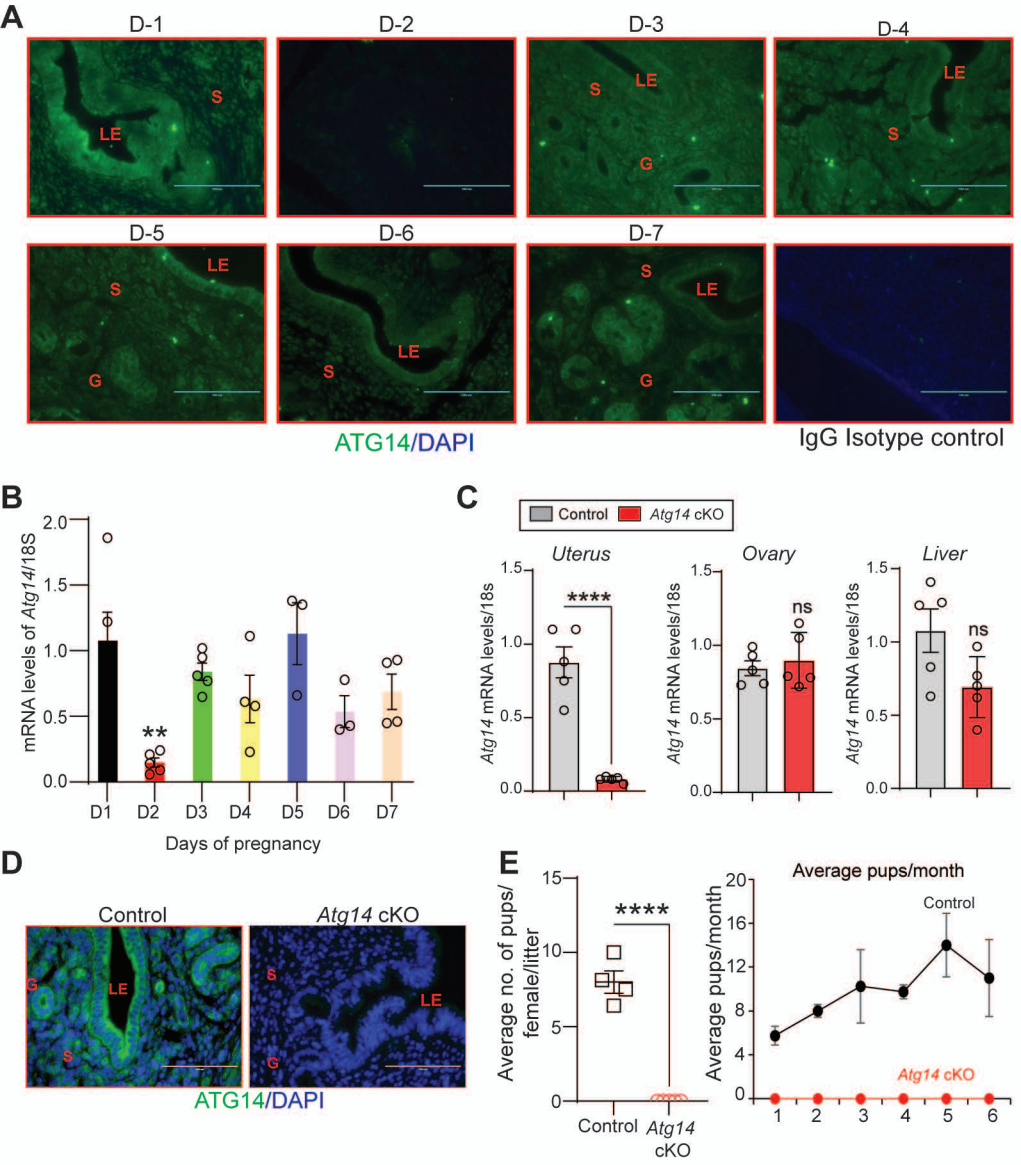
A
D-1
D-2
D-3
D-4
D-5
D-6
D-7
LE
S
G
ATG14/DAPI
IgG Isotype control
B
mRNA levels of Atg14/18S
2.0
1.5
1.0
0.5
0.0
**
D1
D2
D3
D4
D5
D6
D7
Days of pregnancy
C
Control
Atg14 cKO
Uterus
Ovary
Liver
Atg14 mRNA levels/18s
****
ns
D
Control
Atg14 cKO
ATG14/DAPI
E
Average no. of pups/ female/litter
****
Control
Atg14 cKO
Average pups/month
Atg14 cKO

Figure 1

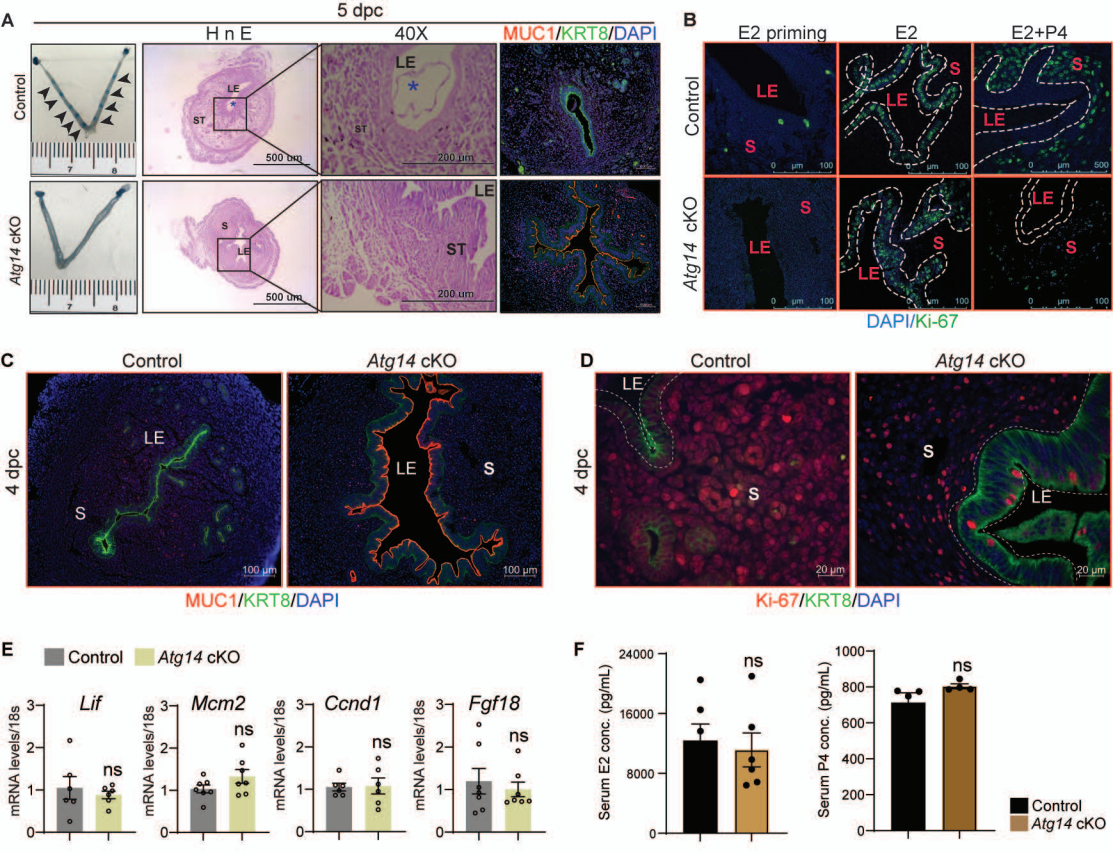
A
5 dpc
H n E
40X
MUC1/KRT8/DAPI
Control
Atg14 cKO
LE
ST
S
500 um
200 µm
B
E2 priming
E2
E2+P4
DAPI/Ki-67
C
Control
Atg14 cKO
4 dpc
100 µm
MUC1/KRT8/DAPI
D
20 µm
Ki-67/KRT8/DAPI
E
Control
Atg14 cKO
mRNA levels/18s
Lif
Mcm2
Ccnd1
Fgf18
ns
F
Serum E2 conc. (pg/mL)
Serum P4 conc. (pg/mL)

Figure 2

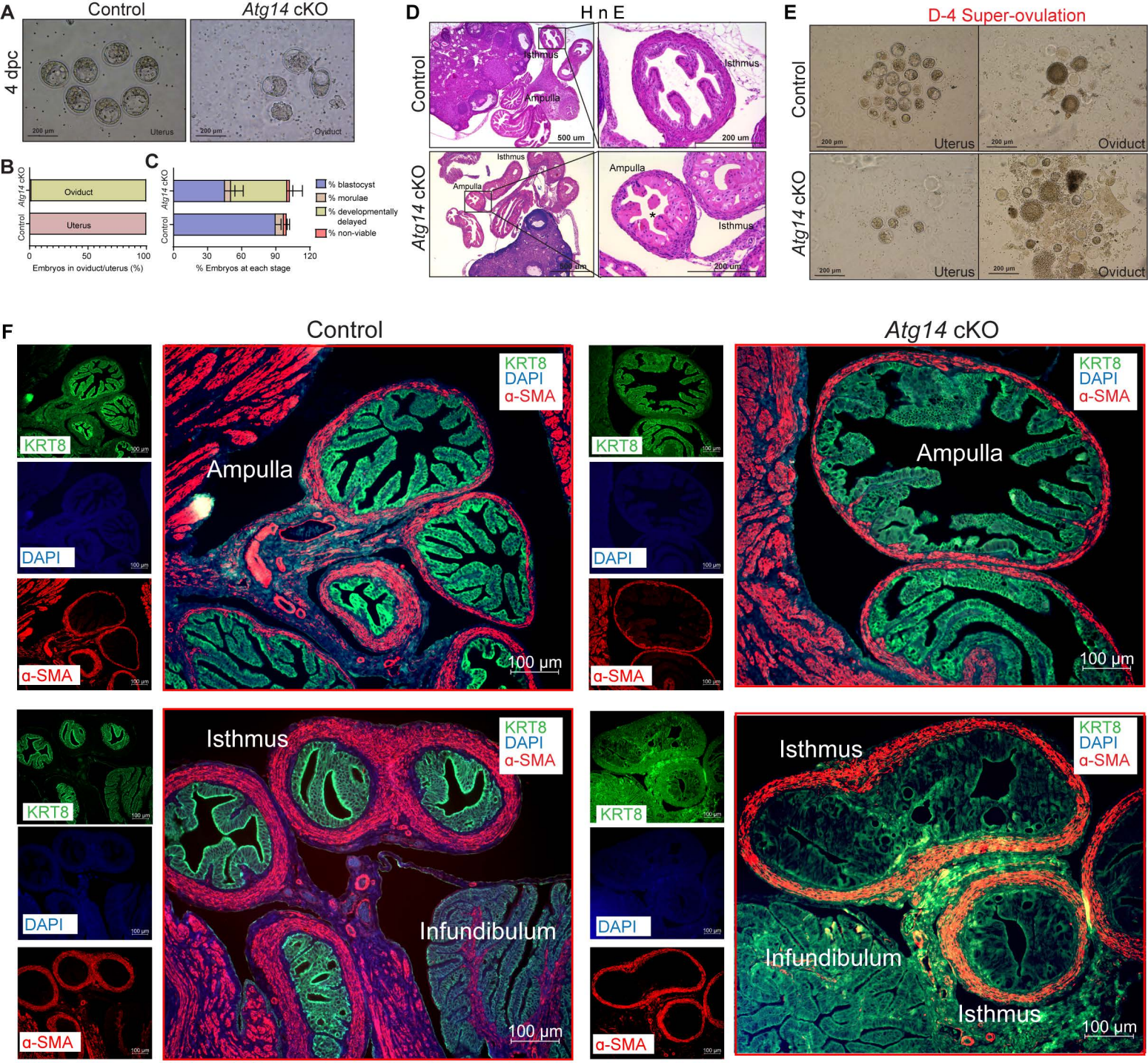
A
Control
Atg14 cKO
4 dpc
200 µm
Uterus
Oviduct
B
Atg14 cKO
Control
Oviduct
Uterus
0
50
100
Embryos in oviduct/uterus (%)
C
0
30
60
90
120
% Embryos at each stage
% blastocyst
% morulae
% developmentally delayed
% non-viable
D
H n E
Isthmus
Ampulla
500 um
200 um
E
D-4 Super-ovulation
F
KRT8
DAPI
α-SMA
100 µm
Infundibulum

Figure 3

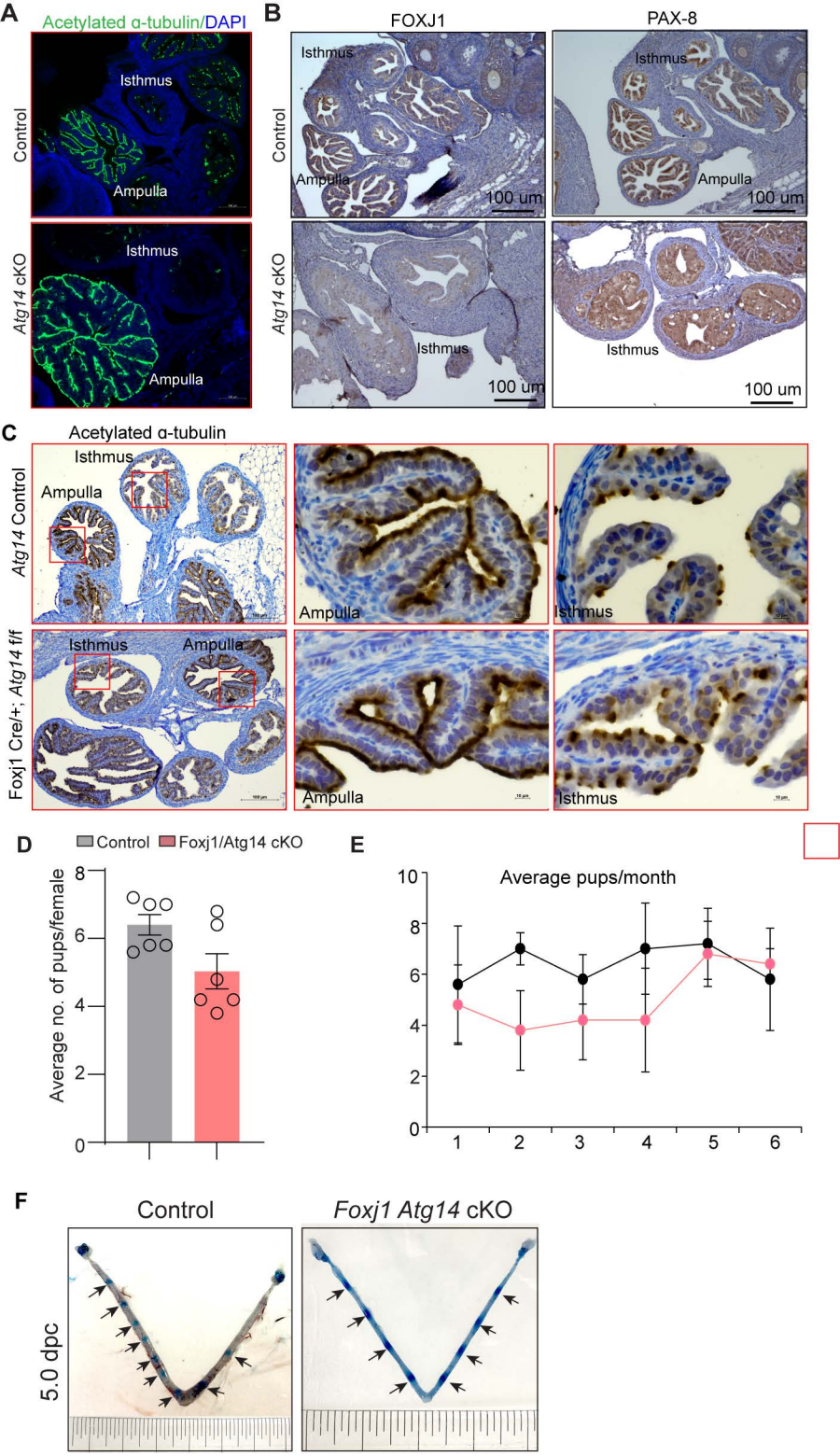
A
Acetylated α-tubulin/DAPI
Control
Isthmus
Ampulla
Atg14 cKO
Isthmus
Ampulla
B
FOXJ1
PAX-8
Control
Isthmus
Ampulla
100 um
Isthmus
Ampulla
100 um
Atg14 cKO
Isthmus
100 um
Isthmus
100 um
C
Acetylated α-tubulin
Atg14 Control
Isthmus
Ampulla
Ampulla
Isthmus
Foxj1 Cre/+; Atg14 f/f
Isthmus
Ampulla
Ampulla
Isthmus
D
Control
Foxj1/Atg14 cKO
Average no. of pups/female
0
2
4
6
8
E
Average pups/month
0
2
4
6
8
10
1
2
3
4
5
6
F
Control
Foxj1 Atg14 cKO
5.0 dpc

Figure 4

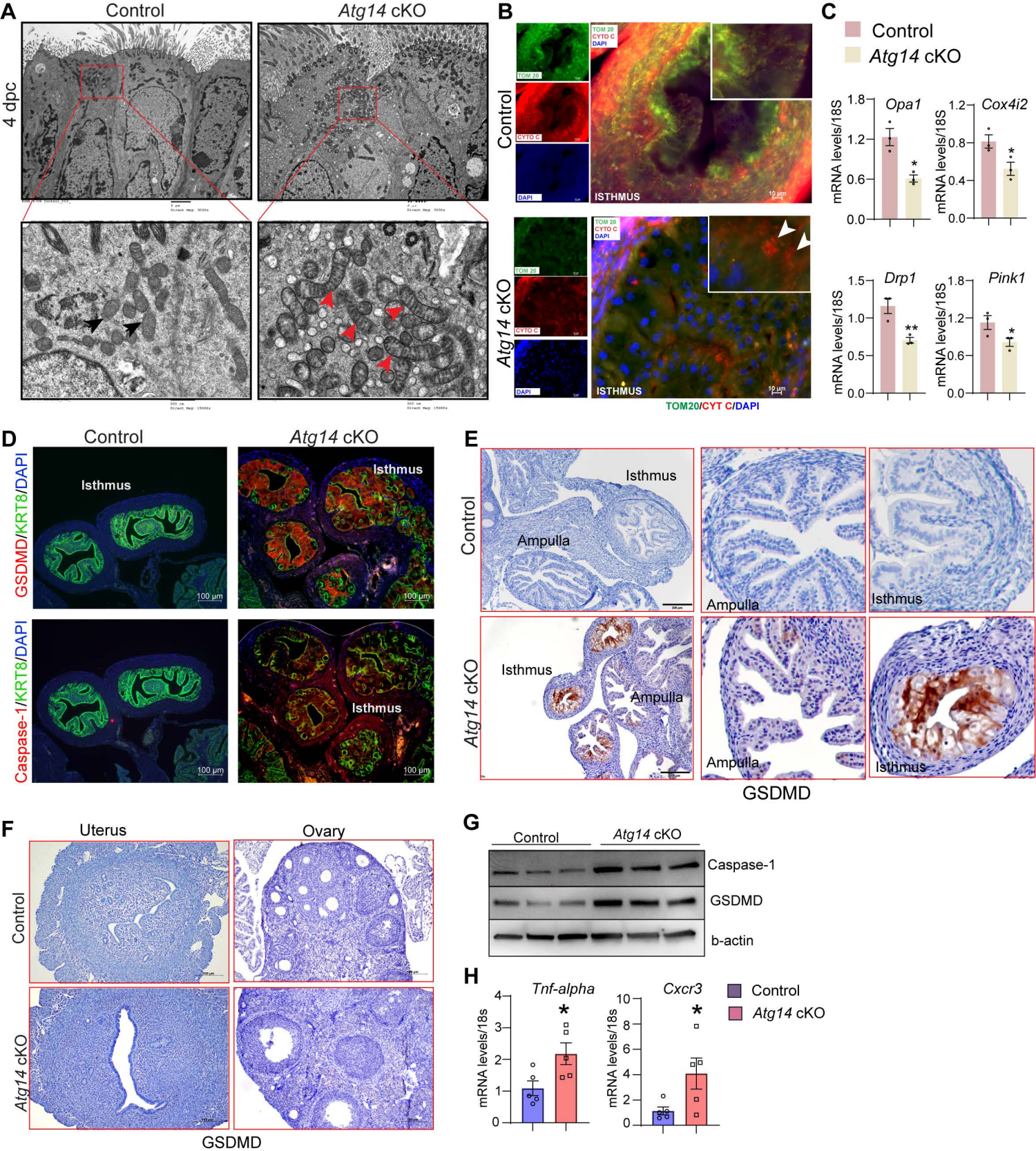
A
Control
Atg14 cKO
4 dpc
B
Control
Atg14 cKO
TOM 20
CYTO C
DAPI
ISTHMUS
10 μm
TOM20/CYT C/DAPI
C
Control
Atg14 cKO
Opa1
Cox4i2
Drp1
Pink1
mRNA levels/18S
D
Control
Atg14 cKO
GSDMD/KRT8/DAPI
Caspase-1/KRT8/DAPI
Isthmus
100 μm
E
Control
Atg14 cKO
Isthmus
Ampulla
GSDMD
F
Uterus
Ovary
Control
Atg14 cKO
GSDMD
G
Control
Atg14 cKO
Caspase-1
GSDMD
b-actin
H
Tnf-alpha
Cxcr3
mRNA levels/18s
Control
Atg14 cKO

Figure 5

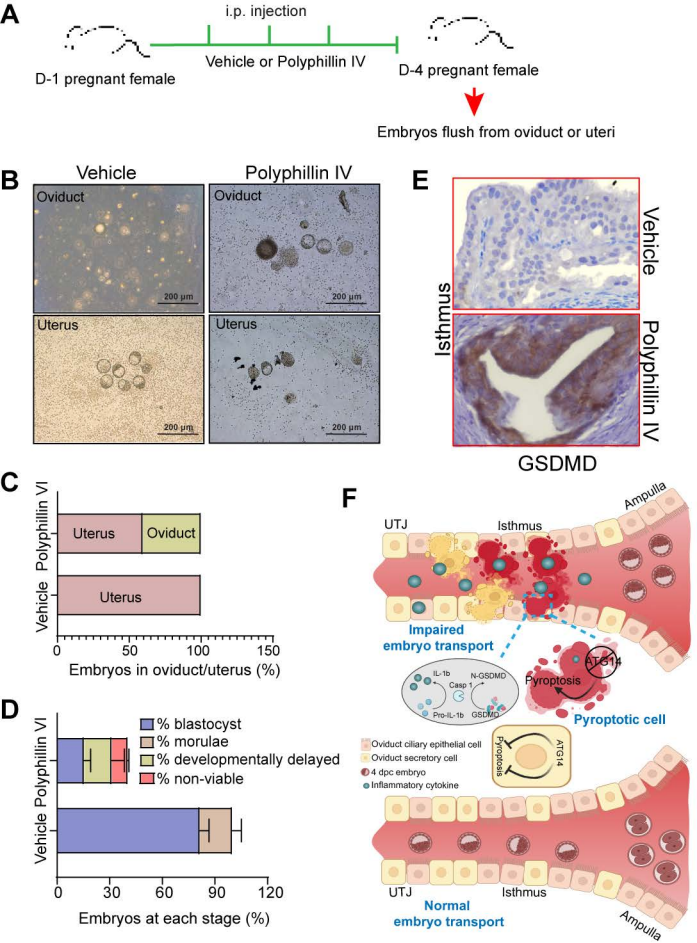
A
i.p. injection
Vehicle or Polyphillin IV
D-1 pregnant female
D-4 pregnant female
Embryos flush from oviduct or uteri
B
Vehicle
Polyphillin IV
Oviduct
Uterus
200 μm
E
Vehicle
Polyphillin IV
Isthmus
GSDMD
C
Polyphillin VI
Vehicle
Uterus
Oviduct
Embryos in oviduct/uterus (%)
D
% blastocyst
% morulae
% developmentally delayed
% non-viable
Embryos at each stage (%)
F
UTJ
Isthmus
Ampulla
Impaired embryo transport
IL-1b
N-GSDMD
Casp 1
Pro-IL-1b
GSDMD
Pyroptosis
ATG14
Pyroptotic cell
Oviduct ciliary epithelial cell
Oviduct secretory cell
4 dpc embryo
Inflammatory cytokine
Normal embryo transport

Figure 6